ENGINEERING

Waveguide metatronics: Lumped circuitry based on structural dispersion

Yue Li,[1,2] Iñigo Liberal,[2] Cristian Della Giovampaola,[2,3] Nader Engheta[2]*

Engineering optical nanocircuits by exploiting modularization concepts and methods inherited from electronics may lead to multiple innovations in optical information processing at the nanoscale. We introduce the concept of "waveguide metatronics," an advanced form of optical metatronics that uses structural dispersion in waveguides to obtain the materials and structures required to construct this class of circuitry. Using numerical simulations, we demonstrate that the design of a metatronic circuit can be carried out by using a waveguide filled with materials with positive permittivity. This includes the implementation of all "lumped" circuit elements and their assembly in a single circuit board. In doing so, we extend the concepts of optical metatronics to frequency ranges where there are no natural plasmonic materials available. The proposed methodology could be exploited as a platform to experimentally validate optical metatronic circuits in other frequency regimes, such as microwave frequency setups, and/or to provide a new route to design optical nanocircuitry.

INTRODUCTION

Electronics, the science and technology aimed to control the flow of electrons, has been one of the main agents of change of the last century. Many influential technologies, such as information and communication technologies, are ultimately supported by an army of small electronic gadgets. Some of the main reasons behind the success and the huge development of electronics are the modularization, simplification, and standardization of circuit elements. That is to say, complex electronic circuits with very diverse functionalities are built by combining individually simple "lumped" components (for example, inductors, capacitors, and resistors) much smaller than the wavelength of operation (1). By contrast, modularization in the field of optics appears at a much higher level, arguably at the device level, leading to discrete elements that have traditionally been much larger than the wavelength of operation, such as mirrors, lenses, and waveguides (2). Therefore, when it comes to subwavelength nanoparticle systems, such as those studied in the fields of near-field optics and nanophotonics, most configurations are typically described by means of intricate many-body scattering problems.

A radically different approach is taken in the field of optical metatronics (3, 4), that is, metamaterial-inspired optical nanocircuitry. Following the success of modularization in electronics, individual nanoparticles are treated as lumped circuit elements (for example, nanocapacitors, nanoinductors, and nanoresistors) whose impedance is defined in terms of how the nanoparticle modifies the flux of the displacement current, $\vec{J}_d = -i\omega\vec{D} = -i\omega\varepsilon_0\varepsilon_r\vec{E}$, as a function of the applied electric potential $\int \vec{E} \cdot d\vec{l}$. Here, "$\varepsilon_r$," represents the relative complex permittivity of the particle. (The time convention $e^{-i\omega t}$ is assumed here.) In addition, in analogy with classical circuit wires, lumped elements in metatronic circuits are usually interconnected via D-dot wires, that is, optical wires designed to confine and "guide" the flow of the displacement current (5). This methodology enables the design of complex nanoparticle systems by using techniques and tools devel-

oped for the design of electronic circuits. For example, several optical nanocircuits with versatile functionalities have already been developed, including filters (6), nanoantennas (7, 8), optical circuits (9) and circuit boards (10, 11), metasurfaces (12), and computational devices (13).

However, the applicability of optical metatronic concepts is limited by the availability of the plasmonic materials required to construct its individual circuit elements. For instance, one requires epsilon-negative (ENG) nanoparticles to construct nanoinductors (3), as well as an epsilon-near-zero (ENZ) host medium to fabricate D-dot wires (10). Both ENG and ENZ responses are present in nature, for example, in materials whose permittivity exhibits a Drude dispersion profile. At optical and infrared frequency domains, Drude dispersion profiles are observed in noble metals (14–19), for example, gold and silver, as well as in transparent conducting oxides (20–25), for example, indium tin oxide and aluminum-doped zinc oxide. Moreover, ENG and ENZ responses can also be engineered by using periodic arrangements forming metamaterials (26–28), although this approach often involves complex and bulky geometries, with intricate phenomena at their boundaries. Here, we investigate, theoretically and numerically, the implementation of metatronic circuits by engineering the structural dispersion in waveguides. In doing so, we extend the paradigm of optical metatronics to frequency ranges where there are no suitable plasmonic materials readily available, for example, microwave and terahertz frequency regimes. The main benefit of this approach is that the reliable, simpler, and cheaper to manufacture experimental setups at microwave frequencies could be used as test beds for optical metatronic concepts. We expect that experimental studies carried out in this platform will consolidate the principles of metatronic circuits and enable further innovations. In principle, this approach could also be adopted to design devices at the microwave frequency regime. However, because of the maturity of microwave integrated circuits, the performance of metatronic devices might not necessarily outperform the existing state-of-the-art microwave devices.

To illustrate our approach, we consider a parallel-plate waveguide (PPW) of height "a," bounded by perfect electric conductor (PEC) walls and excited with a TE_{10} mode with the electric field parallel to the waveguide walls. We assume that the waveguide is filled with a

[1]Department of Electronic Engineering, Tsinghua University, Beijing 100084, China. [2]Department of Electrical and Systems Engineering, University of Pennsylvania, Philadelphia, PA 19104, USA. [3]Department of Information Engineering and Mathematics, University of Siena, I-53100 Siena, Italy.
*Corresponding author. Email: engheta@ee.upenn.edu

material with positive relative permittivity ε_{act} with negligible dispersion over the frequency band of interest. In such a case, the propagation constant β of the TE_{10} mode in the PPW can be written as follows (29): $\beta = k_0 \sqrt{\varepsilon_{eff}}$, where $\varepsilon_{eff} = \varepsilon_{act} - (\pi c/a)^2/\omega^2$ can be regarded as the effective relative permittivity of the TE_{10} mode in terms of propagation. In addition, it can be readily checked that the fields in the middle plane of the waveguide are identical to those of a plane-wave propagating in an equivalent homogeneous medium of relative permittivity ε_{eff} (30). ε_{eff} exhibits a Drude-like dispersion profile that can be adjusted by tuning both the waveguide height a and the relative permittivity of the (positive and dispersionless) material filling the waveguide "ε_{act}." Note that the description of the system based on an effective permittivity is particular of the TE_{10} mode and thus restricted to monomode configurations. Fortunately, it was recently demonstrated theoretically that the excitation of unwanted modes (for example, the TM_{10} mode sharing the same cutoff frequency as the TE_{10} mode) can be mitigated by including a series of thin shorting PEC wires, connecting the top and bottom plates, at the interface between the inhomogeneous materials filling the waveguide (31). In doing so, this approach enables us to extend the notion of an effective permittivity to propagation and scattering processes within inhomogeneously filled waveguides (31). In this manner, by properly selecting the height and the dielectric filling of the waveguide, it is possible to obtain the required effective ENZ and ENG responses at frequency ranges where there are no plasmonic materials and/or to adjust the dispersion profile of an available plasmonic material to a very specific frequency (31).

Previous works have already reproduced some of the unique phenomena associated with ENZ and ENG metamaterials by using waveguide structures (32–35). Here, we numerically demonstrate that structural dispersion enables the design of optical metatronic circuits within a waveguide. To this end, we systematically study the waveguide implementation of all circuit elements, that is, D-dot wires and different lumped elements. We show that all the individual components of a metatronic circuit, as well as their assembly in a single circuit board, can be implemented by engineering the structural dispersion of waveguides. Here, we label this integral implementation of optical metatronic circuits on the basis of structural dispersion as "waveguide metatronics." In the remainder of the article, we present a number of numerical simulations to demonstrate the applicability and performance of the different elements composing waveguide metatronic systems. Without loss of generality, the operating frequency is set at $f_0 = 300$ MHz ($\lambda_0 = 1$ m), where λ_0 is the free space wavelength.

As mentioned earlier, time-harmonic field expressions $e^{-i\omega t}$ are assumed and omitted hereafter.

RESULTS

Overview of a waveguide metatronic circuit
A generic example of a waveguide metatronic circuit is schematically depicted in Fig. 1. The geometry of the device can be explained as follows: First, the whole device is contained within a single PPW designed to work near cutoff. That is, the height of the waveguide a is selected so that the effective permittivity in the waveguide approximates zero ($\varepsilon_{eff} \approx 0$). In this manner, this "metasurface" device is effectively immersed within an ENZ host medium (see Fig. 1B, green), which effectively represents the board over which the circuit will be "printed." Next, the area of the waveguide occupied by the circuit is filled with a dielectric channel such that the effective permittivity in the channel equals one ($\varepsilon_{eff} \approx 1$; see Fig. 1B, gray). In doing so, the dielectric channel effectively behaves as an "air" groove and locally acts as a D-dot wire (5, 10). Next, different "particles" or dielectric slabs can be inserted within the D-dot wire (see Fig. 1B, red, orange, and purple), effectively playing the role of lumped circuit elements that determine the functionality of the circuit. These include capacitors (Re$\{\varepsilon_{eff}\} > 0$), inductors (Re$\{\varepsilon_{eff}\} < 0$), and resistors (Im$\{\varepsilon_{eff}\} \neq 0$), whereas the materials inserted have actually positive values for the real parts of their permittivity functions. The overall circuit is driven by a voltage source implemented as a localized dipole source, for example, a small probe with the polarization selected to excite the TE_{10} mode. To finalize, we introduce thin shorting PEC wires at the interfaces between the different materials filling the waveguide to avoid the mode coupling and the excitation of unwanted modes (see Fig. 1B, brown) (31). In summary, the response of the device can be described via the circuit diagram depicted in Fig. 1C. In this manner, all components of the metatronic circuit are integrated within a single waveguide and implemented by using materials with positive permittivity values. Next, we present a set of representative numerical simulations aimed to assess the performance of the individual components.

Waveguide metatronic D-dot wires
As anticipated, D-dot wires controlling the flow of the displacement current are one of the important parts of optical metatronic circuits. A three-dimensional (3D) schematic view of the simulation setup aimed
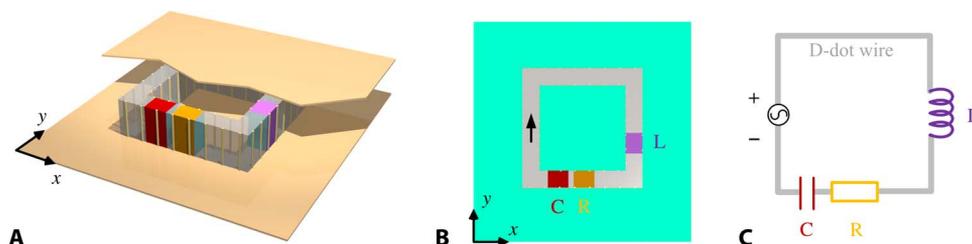
Fig. 1. Conceptual sketch of a waveguide metatronic system. (**A** to **C**) 3D view (A), top view (B), and circuit diagram (C). The system is assumed to be composed of a PPW made of PEC top and bottom plates, operating with its TE_{10} mode near its cutoff that produces an effective ENZ background. A square loop region with a positive dielectric [acting as "D-dot wire" (5, 10)] is inserted in the waveguide. A dipole source [represented by a black arrow in (B)] and three dielectric slabs with different, though all positive real parts of, permittivities are assumed to be in the dielectric loop. The response of the system effectively behaves as a series resistor-inductor-capacitor (RLC) circuit, even though all the materials have positive permittivity.

to evaluate the performance of waveguide metatronic D-dot wires is presented in Fig. 2A. In this case, we use waveguide metatronic D-dot wires of width $0.1\lambda_0$ to form a closed square loop with an average total length of $4\lambda_0$. As anticipated, all material interfaces are surrounded by thin shorting wires, and we found via numerical simulations that PEC wires of diameter $\lambda_0/200$, separated by a pitch of $\lambda_0/20$, suppress the coupling into the TM_{10} mode without significantly affecting the TE_{10} mode. We assume that the waveguide is filled with air ($\varepsilon_{act} = 1$), and we set its height to $a = \lambda_0/2$ so that the effective background relative permittivity approximates to zero ($\varepsilon_{eff} = 0$). Next, the loop surrounded by the thin sorting wires is filled with a dielectric material with relative permittivity $\varepsilon_{act} = 2$, and hence, $\varepsilon_{eff} = 1$. In this manner, the loop operates as an effective air groove within an effective ENZ background, that is, a D-dot wire. The loop is driven by a source selected to excite the TE_{10} mode. In particular, a dipole source, implemented as a discrete port with a voltage source of 1 V, is positioned inside the D-dot wires at the middle plane ($z = a/2$), with its dipole moment parallel to the waveguide walls, as shown in Fig. 1B.

A snapshot of the simulation result of the distribution of the electric field in the middle plane ($z = a/2$) is depicted in Fig. 2B. It can be concluded from the figure that the electric field is longitudinal and uniformly distributed along and within the D-dot wire (except near the source), even though the length of the loop is $4\lambda_0$. Note that the density of the displacement current is given by $\vec{J}_d = -i\omega\varepsilon_0\varepsilon_{eff}\vec{E}$, and thus, although the electric field is nonzero all over the effective ENZ host medium, the effective displacement current remains confined within, and longitudinal to, the D-dot wire ($\varepsilon_{eff} = 0$ outside the wire) and is zero in the background with effective ENZ property. This effect is analogous to the conduction of electrons within high-conductivity wires in electronics, and it also agrees with the D-dot wires in optical metatronics studied by Alù and Engheta (10).

Color maps of the simulation results for the magnitude and phase distributions of the z-component of the magnetic field in the middle plane are shown in Fig. 2 (C and D, respectively). It is worth remarking that the magnetic field in the middle plane at $z = a/2$ is uniform inside the loop of the D-dot wire in both magnitude and phase, even though the simulated region covers several wavelengths. This effect is a property of curl-free linearly polarized magnetic fields (36), and it ratifies that the background medium is acting as an effective ENZ host. We studied the performance of D-dot wires with larger lengths and more intricate shapes (see fig. S1), and it can be concluded that the unique features associated with D-dot are robust against changes in the shape and size of the circuit.

Waveguide metatronic lumped circuit elements
Once the outline of the circuit has been constructed, the next step is to fill it with effective lumped circuit elements. An illustrative example is depicted in Fig. 3A. The geometry is the same as that in Fig. 2A, except that we introduce two different dielectric slabs of length $0.5\lambda_0$ (shown as orange and purple regions in Fig. 3A). Moreover, because we want all the actual materials to be considered in this waveguide to have positive permittivity, in this case, the "ENZ background" region of the waveguide is filled with a material with relative permittivity $\varepsilon_{act} = 3$, and the waveguide height is selected to be $a = 0.2887\lambda_0$, in order for the "background" region of the waveguide to behave again as an ENZ host medium ($\varepsilon_{eff} = 0$). Consequently, the square loop is filled with a material with relative permittivity $\varepsilon_{act} = 4$ to emulate an effective air groove ($\varepsilon_{eff} = 1$). Next, the orange dielectric slab is characterized with relative permittivity $\varepsilon_{act} = 5$ (as a result, $\varepsilon_{eff} = 2$), therefore acting as an effective capacitor, whereas the purple dielectric slab is characterized by permittivity $\varepsilon_{act} = 1$ (with $\varepsilon_{eff} = -2$), thus effectively acting as an inductor. We emphasize that all elements of the waveguide metatronic
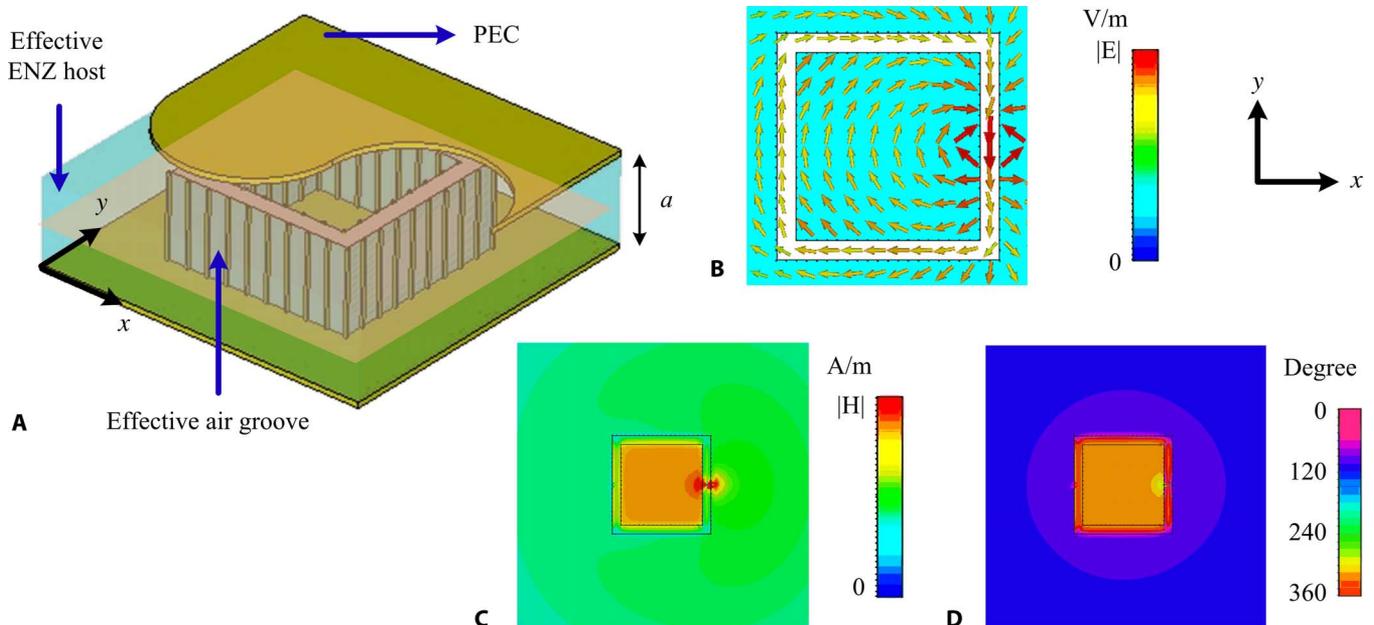
Fig. 2. Simulated performance of a waveguide metatronic D-dot wire. (**A**) 3D view of the simulation setup. (**B**) Snapshot of the simulated results for the electric field distribution on the middle plane ($z = a/2$). (**C** and **D**) Simulation results for magnitude (C) and phase distributions (D) of z-component of magnetic field on the middle plane ($z = a/2$). The circuit is driven by a dipole source, implemented as a discrete port with voltage source of 1 V, positioned inside the D-dot wires at the middle plane ($z = a/2$) with its dipole moment parallel to the waveguide walls and along the D-dot channel.

circuit are assumed to be using readily available materials with positive permittivities.

The simulated performance of the circuit is shown in Fig. 3B, which includes a snapshot of the electric field distribution in the middle plane $z = a/2$. As expected, the effective displacement current is confined in the D-dot wires, which is evidenced by the longitudinal and uniform electric field distribution in the effective air grooves. The top and bottom insets of Fig. 3B include details of the electric field distributions in the capacitor and inductor elements, respectively. It is evident from these figures that the electric field within the capacitor is parallel to the field in the D-dot wires, whereas the field within the inductor is antipodal to it. This property ensures that the displacement current $\vec{J}_d = -i\omega\varepsilon_0\varepsilon_{eff}\vec{E}$ is continuous along the circuit, even after the inclusion of lumped elements. Note also that the electric field is uniformly distributed along the capacitor and inductor elements. Therefore, it can be concluded that, because of the phase uniformity induced by the ENZ host, these dielectric slabs play the role of lumped elements (as compared with the effectively long wavelength in the effective ENZ region) despite having a relative long length of $0.5\lambda_0$.

Furthermore, the impedance values of the dielectric slabs can be defined in accordance to basic circuit theory. To guide our discussion, sketches of the theoretical distributions of the fields in the capacitor and inductor circuit elements are depicted in Fig. 3 (C and D, respectively). In essence, we describe the response of the circuit elements with respect to the fields in the middle plane $z = a/2$, where the notion of an effective permittivity works at a local field level, leading to 2D impedance terms per unit length with the unit of ohm·m. This approach is ultimately valid due to the enforced monomode configuration, where the variation along the z axis is fixed by the TE_{10} mode profile so that the analysis is reduced to a 2D problem. Hence, we

consider each element as an effective 2D dielectric slab of length l and width t. As confirmed by our previous numerical simulations, the electric field in the middle plane $z = a/2$ is characterized by a uniform distribution with constant value E_0, longitudinal to width t. Thus, the total surface displacement current (per unit length in the z direction) flowing through the circuit elements is given by $I_s = -i\omega\varepsilon_0\varepsilon_{eff}E_0t$ (A/m), whereas the voltage across the impedance element is $V = E_0l$. Therefore, the 2D impedance of the dielectric slab can be simply written as follows

$$Z = \frac{V}{I_s} = \frac{l}{-i\omega\varepsilon_0\varepsilon_{eff}t} \tag{1}$$

On the one hand, it is clear from Eq. 1 that dielectric slabs with positive permittivity behave as capacitors with impedance (ohm·m) and capacitance (F/m)

$$Z = (-i\omega C)^{-1}, C = \varepsilon_0\varepsilon_{eff}t/l \tag{2}$$

On the other hand, the response of a dielectric slab with negative effective permittivity equals that of an inductor with 2D impedance (ohm·m) and inductance (H·m)

$$Z = -i\omega L, L = -l/(\omega^2\varepsilon_0\varepsilon_{eff}t) \tag{3}$$

We validate this approach by numerically computing via field integration the 2D impedance values of circuit elements with different
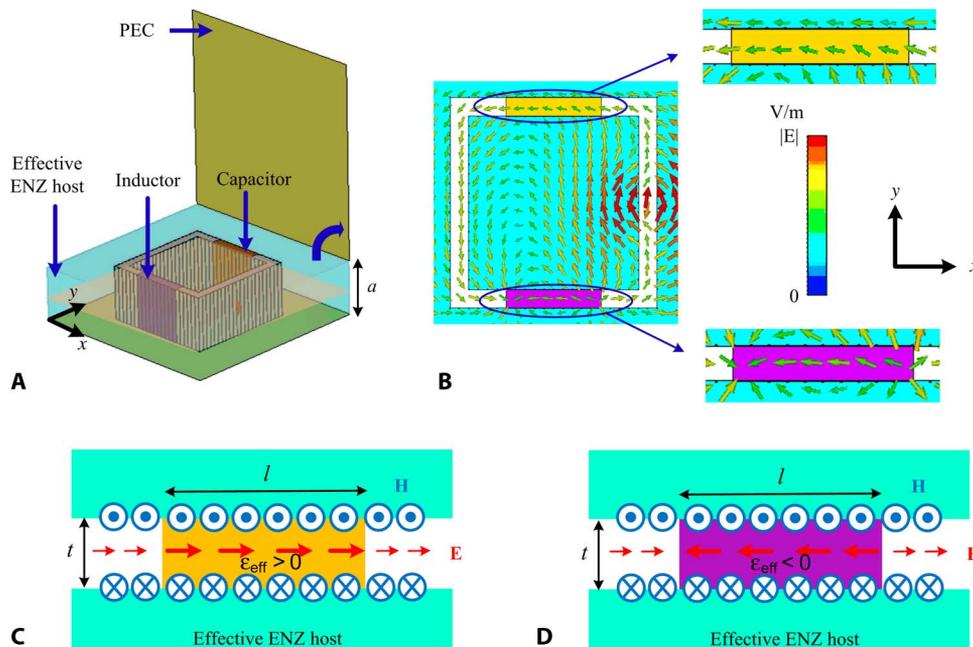
Fig. 3. Idea for implementation of lumped circuit elements in waveguide metatronics using only materials with positive permittivities. (**A**) 3D schematic view of the simulation setup. (**B**) Snapshot of the simulation results for the electric field distribution on the middle plane ($z = a/2$). Insets: Zoom in on the simulated electric field distribution in the capacitor (top) and inductor (bottom) circuit elements. (**C** and **D**) Sketches of the theoretical electric and magnetic field distributions in the capacitor (C) and inductor (D) elements.

values of length, width, and permittivity, including those studied in Fig. 3. The results are gathered in fig. S2, and it can be concluded that there is an excellent agreement between the theoretical and numerical results. Therefore, the slabs introduced in the D-dot wires, though not electrically small (with respect to the free space wavelength), can be effectively treated as lumped elements in the ENZ host.

Metatronic circuits interacting with a propagating mode

Aside from their operation within a circuit board, metatronic circuits can also be used as discrete components in the design of filters and metasurfaces. Here, we numerically assess the performance of resonant series and parallel LC circuits embedded in a waveguide. A 3D view of the simulation setup is depicted in Fig. 4A. The geometry consists of an incident x-polarized TE_{10} mode propagating along a rectangular waveguide of length $2\lambda_0$ (y axis), width $0.1\lambda_0$ (x axis), and height $a = 0.15\lambda_0$ (z axis) made of PEC walls. The waveguide is filled with a dielectric material with relative permittivity $\varepsilon_{act} = 11$ so that effective permittivity is near (though slightly larger than) zero $\varepsilon_{eff} \approx 0$. This ensures that all interactions within the waveguide have a quasi-static character while still allowing for the propagation of the incident TE_{10} mode.

A waveguide metatronic circuit is positioned in the center of the waveguide to control the reflection and transmission properties in the waveguide (see Fig. 4A, green component marked by a blue circle). In particular, the reflection coefficient is given by $R = -Z_0/(2Z_S + Z_0)$, where Z_S is impedance of the waveguide metatronic circuit and Z_0 is the characteristic impedance of the waveguide. For example, when the circuit consists of a single slab, its impedance can be simply calculated by using Eq. 1. We numerically calculated the values of capacitance and inductance implemented with single slabs, as well as the transmission/reflection properties of those circuits (see fig. S3). The results of the numerical simulations agree with the circuit formalism.

Next, we move to the design of the LC circuits by arranging them in series and parallel configurations as schematically depicted in Fig. 4 (B and C). The thickness of the individual elements is set to $0.01\lambda_0$. In addition, the capacitor is composed of a dielectric with relative actual permittivity $\varepsilon_{act} = 19$ (so the effective value of $\varepsilon_{C,eff} = 8$), whereas the inductor is composed of a dielectric with relative actual permittivity
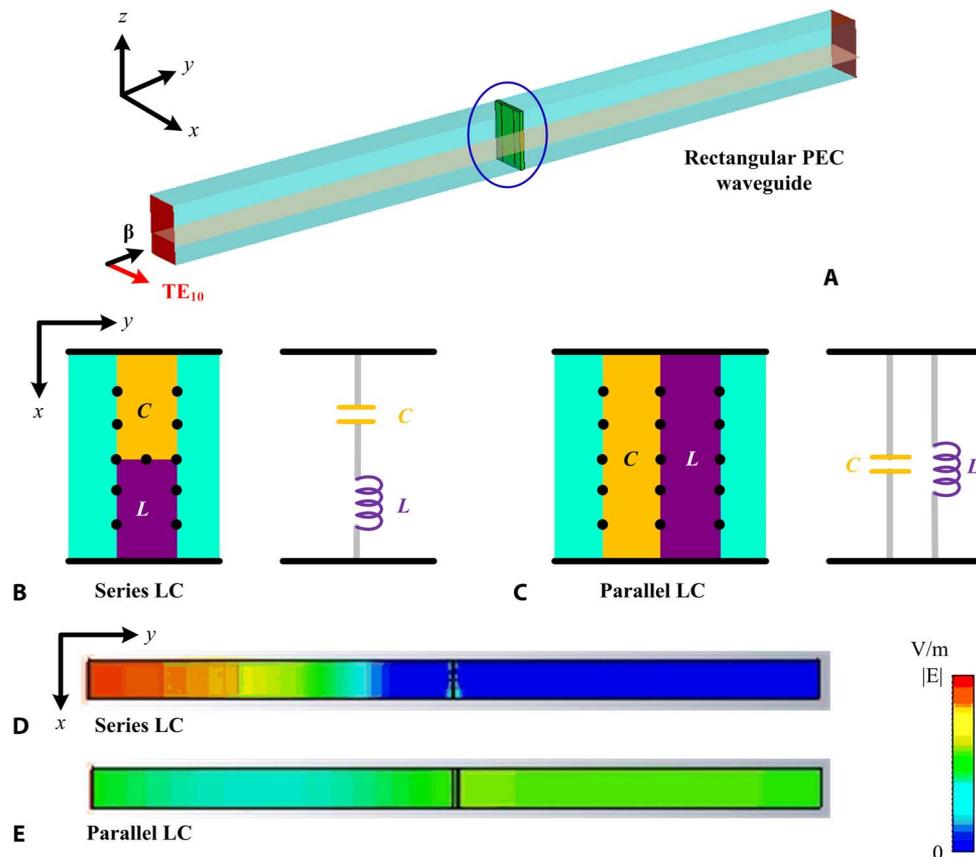
Fig. 4. Idea for implementation of LC circuits based on waveguide metatronics using only materials with positive permittivities. (**A**) 3D view of the simulation setup. The system is composed of a rectangular PEC waveguide with a TE_{10} incident mode propagating slightly above its cutoff. The LC circuit (shown in green) is marked by a blue circle. (**B** and **C**) Top views and associated circuit diagrams of the series (B) and parallel (C) LC circuits all with only materials with positive dielectric. The permittivities of the capacitor ($\varepsilon_{act} = 19$ and $\varepsilon_{C,eff} = 8$) and inductor ($\varepsilon_{act} = 3$ and $\varepsilon_{L,eff} = -8$) elements are selected so that the effective LC circuits operate at resonance $\omega L = 1/(\omega C)$. (**D** and **E**) Color map of the simulation results for the electric field magnitude distributions for the series (D) and parallel (E) LC circuits on the middle plane in (A) ($z = a/2$). The numerical simulations demonstrate that, as expected, the series LC circuit responds as a short circuit that blocks the propagation of the incident wave, whereas the parallel LC circuit responds as an open circuit with no significant impact on the propagation of the incident wave.

$\varepsilon_{act} = 3$ (thus, $\varepsilon_{L,eff} = -8$). This configuration ensures that the impedances are balanced, that is, $Z_L = -Z_C$, and hence, the series and parallel circuits are at resonance. The simulation results for performance of the series and parallel LC circuits are shown in Fig. 4 (D and E), which include color maps of the electric field magnitude distribution in the middle plane of the waveguide ($z = a/2$). The numerical results can be readily explained on the basis of the circuit theory. On the one hand, the series LC circuit is characterized by impedance $Z_S = Z_L + Z_C \rightarrow 0$, and hence, the reflection coefficient equals −1. That is, the series LC circuit behaves as a short circuit that reflects most of the incident energy. On the other hand, the parallel LC circuit is characterized by impedance $Z_S = \left(Z_L^{-1} + Z_C^{-1}\right)^{-1} \rightarrow \infty$, and consequently, the reflection coefficient goes to zero. Thus, most of the energy is transmitted through the waveguide metatronic circuit.

DISCUSSION

In conclusion, we have introduced the concept of waveguide metatronics, a microwave version of optical metatronics in which structural dispersion is used to emulate the materials required to construct this class of circuitry. This paradigm enables us to extrapolate metatronic concepts to frequency ranges where there are no naturally and easily available plasmonic materials, and thus, only materials with positive permittivity can be used. In doing so, we open the possibility of using reliable microwave frequency experimental setups as test beds of optical metatronic concepts. We have demonstrated using numerical simulations that all the constituents of a metatronic circuit can be integrated within a single waveguide filled with only materials with positive permittivity.

For the sake of simplicity, in this analysis, we considered lossless materials, and the frequency of operation was set to 300 MHz ($\lambda_0 = 1$ m). However, the performance of the system is expected to be robust against dissipation losses in such frequencies, and it could be easily scaled to certain higher frequency ranges. For instance, figs. S4, S5, and S9 present the numerical simulation of the devices studied in Figs. 2 and 4A, respectively, but substituting the PEC boundaries and shorting wires by copper with conductivity ($\sigma = 5.8 \times 10^7$ S/m), and including losses in the dielectrics through a loss tangent $\tan\delta = 0.001$. We find that finite conductivity has a negligible impact on the performance of the devices in this frequency range. Moreover, additional preliminary simulations presented in fig. S11 indicate that the proposed systems could be scaled up to tetrahertz (THz) before the operational principle is lost. The design, optimization, and quantitative estimation of the performance in these frequency ranges are beyond the scope of this work.

Similarly, this study was conducted for time-harmonic fields, and the aspects related to bandwidth were not addressed here. In practice, we expect that the bandwidth of the system will be limited by the dispersion of the platform hosting the lumped elements because the metatronic lumped elements themselves may potentially be inherently broadband (3). Preliminary simulations presented in figs. S4 to S8 indicate that a conservative estimate of the bandwidth of waveguide D-dot wires might be around 5%. On the other hand, the bandwidth of the system may be substantially wider for the lumped elements themselves inserted in the waveguide and interacting with a propagating TE$_{10}$ mode, as shown in figs. S9 and S10. In both cases, it is found that the operational bandwidth can easily host the resonant phenomena and functionality of LC tanks. A more comprehensive analysis and optimization of the bandwidth, as well as the signal processing capabilities within this platform, are left for future efforts.

To finalize, we emphasize that although the presented results are based on parallel-plate and rectangular waveguides, the proposed methodology can be straightforwardly extrapolated to some other bounded guiding systems with structure-dependent dispersion profiles. Similarly, the same methodology can be adopted in the design of more complex circuits with advanced functionalities.

MATERIALS AND METHODS

The numerical results illustrated in this study were obtained using the commercial software CST Microwave Studio. Specifically, we used the time-domain solver with hexahedral meshing. For the host medium and groove dielectric, the maximum meshing element size was set to $\lambda_0/100$. For the lumped elements, we used a denser local mesh with a maximum element size of $\lambda_0/200$. For the simulations in Figs. 2 and 3, an electric dipole moment was set as a voltage source with input voltage of 1 V. The length of the dipole source was $\lambda_0/50$. The total size of the host medium inside the waveguide was $6\lambda_0 \times 6\lambda_0$ in the xy plane.

SUPPLEMENTARY MATERIALS

Supplementary material for this article is available at http://advances.sciencemag.org/cgi/content/full/2/6/e1501790/DC1

fig. S1. Field distributions in waveguide metatronic D-dot wires.
fig. S2. Impedance of lumped elements within a D-dot wire.
fig. S3. Lumped circuit elements embedded within a rectangular waveguide.
fig. S4. Frequency response of waveguide metatronic D-dot wires.
fig. S5. Normalized frequency response of waveguide metatronic D-dot wires.
fig. S6. Frequency response of lumped elements within a D-dot wire.
fig. S7. Frequency response of a series LC tank within a D-dot wire.
fig. S8. Impedance of the series LC tank within a D-dot wire.
fig. S9. Frequency response of the series LC tank embedded in a waveguide.
fig. S10. Frequency response of the series LC tank within the waveguide.
fig. S11. Field distributions in waveguide metatronic D-dot wires at THz and infrared frequencies.

REFERENCES AND NOTES

1. C. K Alexander, M. N. O. Sadiku, *Fundamentals of Electric Circuits* (McGraw-Hill Education, New York, ed. 5, 2012).
2. B. E. A. Saleh, M. C. Teich, *Fundamentals of Photonics* (John Wiley & Sons, Hoboken, NJ, ed. 2, 2007).
3. N. Engheta, A. Salandrino, A. Alù, Circuit elements at optical frequencies: Nanoinductors, nanocapacitors, and nanoresistors. *Phys. Rev. Lett.* **95**, 095504 (2005).
4. N. Engheta, Circuits with light at nanoscales: Optical nanocircuits inspired by metamaterials. *Science* **317**, 1698–1702 (2007).
5. B. Edwards, N. Engheta, Experimental verification of displacement-current conduits in metamaterials-inspired optical circuitry. *Phys. Rev. Lett.* **108**, 193902 (2012).
6. Q. Zhang, L. Bai, Z. Bai, P. Hu, C. Liu, Equivalent-nanocircuit-theory-based design to infrared broad band-stop filters. *Opt. Express* **23**, 8290–8297 (2015).
7. A. Alù, N. Engheta, Tuning the scattering response of optical nanoantennas with nanocircuit loads. *Nat. Photonics* **2**, 307–310 (2008).
8. J.-S. Huang, T. Feichtner, P. Biagioni, B. Hecht, Impedance matching and emission properties of nanoantennas in an optical nanocircuit. *Nano Lett.* **9**, 1897–1902 (2009).
9. J. Shi, F. Monticone, S. Elias, Y. Wu, D. Ratchford, X. Li, A. Alù, Modular assembly of optical nanocircuits. *Nat. Commun.* **5**, 3896 (2014).
10. A. Alù, N. Engheta, All optical metamaterial circuit board at the nanoscale. *Phys. Rev. Lett.* **103**, 143902 (2009).
11. L. Min, L. Huang, All-semiconductor metamaterial-based optical circuit board at the microscale. *J. Appl. Phys.* **118**, 013104 (2015).

12. F. Monticone, N. M. Estakhri, A. Alù, Full control of nanoscale optical transmission with a composite metascreen. *Phys. Rev. Lett.* **110**, 203903 (2013).

13. A. Silva, F. Monticone, G. Castaldi, V. Galdi, A. Alù, N. Engheta, Performing mathematical operations with metamaterials. *Science* **343**, 160–163 (2014).

14. P. B. Johnson, R. W. Christy, Optical constants of the noble metals. *Phys. Rev. B* **6**, 4370 (1972).

15. M. A. Ordal, L. L. Long, R. J. Bell, R. R. Bell, R. W. Alexander, C. A. Ward, Optical properties of the metals Al, Co, Cu, Au, Fe, Pb, Ni, Pd, Pt, Ag, Ti, and W in the infrared and far infrared. *Appl. Opt.* **22**, 1099–1020 (1983).

16. J. B. Pendry, A. J. Holden, W. J. Stewart, I. Youngs, Extremely low frequency plasmons in metallic mesostructures. *Phys. Rev. Lett.* **76**, 4773–4776 (1996).

17. T. Hayakawa, S. T. Selvan, M. Nogami, Field enhancement effect of small Ag particles on the fluorescence from Eu^{3+}-doped SiO_2 glass. *Appl. Phys. Lett.* **74**, 1513–1515 (1999).

18. N. V. Smith, Classical generalization of the Drude formula for the optical conductivity. *Phys. Rev. B* **64**, 155106 (2001).

19. K. Lee, S. Cho, S. H. Park, A. J. Heeger, C.-W. Lee, S.-H. Lee, Metallic transport in polyaniline. *Nature* **441**, 65–68 (2006).

20. J. Steinhauser, S. Fäy, N. Oliveira, E. Vallat-Sauvain, D. Zimin, U. Kroll, C. Ballif, Electrical transport in boron-doped polycrystalline zinc oxide thin films. *Phys. Status Solidi Appl. Mater. Sci.* **205**, 1983–1987 (2008).

21. A. Boltasseva, H. A. Atwater, Low-loss plasmonic metamaterials. *Science* **331**, 290–291 (2011).

22. J. B. Khurgin, A. Boltasseva, Reflecting upon the losses in plasmonics and metamaterials. *MRS Bull.* **37**, 768–779 (2012).

23. J. Kim, G. V. Naik, N. K. Emani, U. Guler, A. Boltasseva, Plasmonic resonances in nanostructured transparent conducting oxide films. *IEEE J. Sel. Top. Quantum Electron* **19**, 4601907 (2013).

24. W. Su, K. Song, D. Huo, B. Li, Analysis of correlation between electrical and infrared optical properties of anatase Nb doped TiO_2 films. *Curr. Appl. Phys.* **13**, 556–561 (2013).

25. T. Wang, M. Zalkovskij, K. Iwaszczuk, A. V. Lavrinenko, G. V. Naik, J. Kim, Ultrabroadband terahertz conductivity of highly doped ZnO and ITO. *Opt. Mater. Express* **5**, 566–575 (2015).

26. J. B. Pendry, L. Martín-Moreno, F. J. Garcia-Vidal, Mimicking surface plasmons with structured surfaces. *Science* **305**, 847–848 (2004).

27. S. A. Tretyakov, *Analytical Modeling in Applied Electromagnetics* (Artech House, Norwood, MA, 2003).

28. W. Cai, V. M. Shalaev, *Optical Metamaterials: Fundamentals and Applications* (Springer, New York, 2010).

29. W. Rotman, Plasma simulation by artificial dielectrics and parallel-plate media. *IRE Trans. Antennas Propag.* **10**, 82–95 (1962).

30. D. Pozar, *Microwave engineering* (John Wiley & Sons, New York, ed. 4, 2011).

31. C. Della Giovampaola, N. Engheta, Plasmonics without negative dielectrics. *Phys. Rev. B* **93**, 195152 (2016).

32. R. Marqués, J. Martel, F. Mesa, F. Medina, Left-handed-media simulation and transmission of EM waves in subwavelength split-ring-resonator-loaded metallic waveguides. *Phys. Rev. Lett.* **89**, 183901 (2002).

33. S. Hrabar, J. Bartolic, Z. Sipus, Waveguide miniaturization using uniaxial negative permeability metamaterial. *IEEE Trans. Antennas Propag.* **53**, 110–119 (2005).

34. B. Edwards, A. Alù, M. E. Young, M. Silveirinha, N. Engheta, Experimental verification of epsilon-near-zero metamaterial coupling and energy squeezing using a microwave waveguide. *Phys. Rev. Lett.* **100**, 033903 (2008).

35. Y. Li, N. Engheta, Supercoupling of surface waves with ε-near-zero metastructures. *Phys. Rev. B* **90**, 201107 (2014).

36. M. G. Silveirinha, N. Engheta, Tunneling of electromagnetic energy through subwavelength channels and bends using ε-near-zero materials. *Phys. Rev. Lett.* **97**, 157403 (2006).

Citation: Y. Li, I. Liberal, C. Della Giovampaola, N. Engheta, Waveguide metatronics: Lumped circuitry based on structural dispersion. *Sci. Adv.* **2**, e1501790 (2016).

***The following resources related to this article are available online at
http://advances.sciencemag.org. (This information is current as of June 10, 2016):***

Updated information and services, including high-resolution figures, can be found in the online version of this article at:
http://advances.sciencemag.org/content/2/6/e1501790.full

Supporting Online Material can be found at:
http://advances.sciencemag.org/content/suppl/2016/06/07/2.6.e1501790.DC1

This article **cites 31 articles,** 4 of which you can be accessed free:
http://advances.sciencemag.org/content/2/6/e1501790#BIBL